Inorganic Chemistry
Article

Inorg. Chem. **2010**, *49*, 7565–7576 **7565**
DOI: 10.1021/ic100937h

Nature of Magnetic Interactions in 3D $\{[M^{II}(pyrazole)_4]_2[Nb^{IV}(CN)_8]\cdot 4H_2O\}_n$ (M = Mn, Fe, Co, Ni) Molecular Magnets

Dawid Pinkowicz,*[†] Robert Pełka,*[‡] Olga Drath,[†] Wojciech Nitek,[†] Maria Bałanda,[‡] Anna Małgorzata Majcher,[§] Giordano Poneti,[⊥] and Barbara Sieklucka*[†]

[†]*Faculty of Chemistry, Jagiellonian University, Ingardena 3, 30-060 Kraków, Poland,* [‡]*H. Niewodniczański Institute of Nuclear Physics PAN, Radzikowskiego 152, 31-342 Kraków, Poland,* [§]*Institute of Physics, Jagiellonian University, Reymonta 4, 30-059 Kraków, Poland, and* [⊥]*Laboratory of Molecular Magnetism (LAMM), Department of Chemistry, Ugo Schiff and INSTM Research Unit, University of Florence, Via della Lastruccia 3−13, 50019 Sesto Fiorentino, Florence, Italy*

Received May 11, 2010

The self-assembly of $[Nb^{IV}(CN)_8]^{4-}$ with different 3d metal centers in an *aqueous* solution and an excess of pyrazole resulted in the formation of four 3D isostructural compounds $\{[M^{II}(pyrazole)_4]_2[Nb^{IV}(CN)_8]\cdot 4H_2O\}_n$, where M^{II} = Mn, Fe, Co, and Ni for **1**−**4**, respectively. All four assemblies crystallize in the same $I4_1/a$ space group and show identical cyanido-bridged structures decorated with pyrazole molecules coordinated to M^{II} centers. All four compounds show also long-range magnetic ordering below 24, 8, 6, and 13 K, respectively. A thorough analysis of the structural and magnetic data utilizing the molecular field model has allowed for an estimation of the values of coupling constants J_{M-Nb} attributed to the one type of $M^{II}-NC-Nb^{IV}$ linkage existing in **1**−**4**. The J_{M-Nb} values increase monotonically from −6.8 for **1** through −3.1 for **2** and +3.5 for **3**, to +8.1 cm^{-1} for **4** and are strongly correlated with the number of unpaired electrons on the M^{II} metal center. Average orbital contributions to the total exchange coupling constants J_{M-Nb} have also been identified and calculated: antiferromagnetic $J_{AF} = -21.6$ cm^{-1} originating from the d_{xy}, d_{xz}, and d_{yz} orbitals of M^{II} and ferromagnetic $J_F = +15.4$ cm^{-1} originating from d_{z^2} and $d_{x^2-y^2}$ orbitals of M^{II}. Antiferromagnetic interaction is successively weakened in the **1**−**4** row with each additional electron on the t_{2g} level, which results in a change of the sign of J_{M-Nb} and the nature of long-range magnetic ordering from ferrimagnetic in **1** and **2** to ferromagnetic in **3** and **4**.

1. Introduction

Hybrid organic−inorganic molecular magnets exhibiting extended 3D coordination frameworks have recently attracted tremendous interest because of their captivating structural topologies and wide potential applications as functional materials with physical and chemical properties including porosity,[1] reversible sorption, sensing of target molecules, pyroelectricity, optical activity, nonlinear optics, etc.

Formulation of the rules and concepts governing relations between architectures and properties[2−4] allows a rational approach to the design and synthesis of the next generation of molecular magnets that show significant improvement of their magnetic properties (high-T_c molecular magnets[5]) or combine multiple closely intertwined functions that give rise to multifunctional molecular magnetic materials (4Ms: magnetic sponges,[6] photoinduced magnets,[7] conducting magnets,[8] spin-crossover multifunctional materials,[9] etc.)

---

*To whom correspondence should be addressed. E-mail: pinkowic@chemia.uj.edu.pl (D.P.), robert.pelka@ifj.edu.pl (R.P.), barbara.sieklucka@uj.edu.pl (B.S.).

(1) Férey, G. *Chem. Soc. Rev.* **2008**, *37*, 191–214.

(2) O'Keeffe, M.; Eddaoudi, M.; Li, H.; Reineke, T.; Yaghi, O. M. *J. Solid State Chem.* **2000**, *152*, 3–20.

(3) Férey, G. *J. Solid State Chem.* **2000**, *152*, 37–53.

(4) Verdaguer, M.; Girolami, G. Magnetic Prussian Blue Analogs. In *Magnetism: Molecules to Materials V*; Miller, J. S., Drillon, M., Eds.; Wiley-VCH Verlag GmbH & Co. KGaA: Weinheim, Germany, 2004; Chapter 9.

(5) (a) Entley, W. R.; Girolami, G. S. *Inorg. Chem.* **1994**, *33*, 5165–5166. (b) Ferlay, S.; Mallah, T.; Ouahès, R.; Veillet, P.; Verdaguer, M. *Inorg. Chem.* **1999**, *38*, 229–234. (c) Ferlay, S.; Mallah, T.; Ouahès, R.; Veillet, P.; Verdaguer, M. *Nature* **1995**, *378*, 701.

(6) (a) Larionova, J.; Chavan, S. A.; Yakhmi, J. V.; Gulbrandsen Frøystein, A.; Sletten, J.; Sourisseau, C.; Kahn, O. *Inorg. Chem.* **1997**, *36*, 6374–6381. (b) Kahn, O.; Larionova, J.; Yakhmi, J. V. *Chem.—Eur. J.* **1999**, *5*, 3443–3449.

(7) (a) Ohkoshi, Sh.; Hashimoto, K. *J. Photochem. Photobiol. C: Photochem. Rev.* **2001**, *2*, 71–88. (b) Shimamoto, N.; Ohkoshi, Sh.; Sato, O.; Hashimoto, K. *Inorg. Chem.* **2002**, *41*, 678–684. (c) Bleuzen, A.; Marvaud, V.; Mathoniere, C.; Sieklucka, B.; Verdaguer, M. *Inorg. Chem.* **2009**, *48*, 3453–3466.

(8) (a) Uji, S.; Shinagawa, H.; Terashima, T.; Yakabe, T.; Terai, Y.; Tokumoto, M.; Kobayashi, A.; Tanaka, H.; Kobayashi, H. *Nature* **2001**, *410*, 908. (b) Hiraga, H.; Miyasaka, H.; Clérac, R.; Fourmigué, M.; Yamashita, M. *Inorg. Chem.* **2009**, *48*, 2887–2898.

(9) (a) Cobo, S.; Ostrovskii, D.; Bonhommeau, S.; Vendier, L.; Molnár, G.; Salmon, L.; Tanaka, K.; Bousseksou, A. *J. Am. Chem. Soc.* **2008**, *130*, 9019–9024. (b) Ohba, M.; Yoneda, K.; Agustí, G.; Muñoz, C.; Gaspar, A. B.; Real, J. A.; Yamasaki, M.; Ando, H.; Nakao, Y.; Sakaki, S.; Kitagawa, S. *Angew. Chem., Int. Ed.* **2009**, *48*, 4767–4771.

and new phenomena like magnetization-induced second-harmonic generation in pyroelectric magnets[10] or magneto-chiral dichroism in chiral magnets.[11]

In the previous reports on hybrid molecular magnets of $M^{II}-(L)-[Nb^{IV}(CN)_8]$ type (M^{II} = V, Mn, Fe, Ni; L = nonmagnetic organic ligand), it was shown that L affects the magnetic properties indirectly by introducing additional interaction pathways and controlling the overall dimensionality/connectivity type of the resulting network from discrete 0D high-spin (HS) clusters,[12a,b] to 1D cyanido-bridged chains,[12b,c] to 3D networks.[13−15] The change of the paramagnetic M^{II} center, on the contrary, has a direct impact on the occurrence of magnetic anisotropy,[12b,13d] spin crossover,[14b] or high ordering temperatures.[14c] It was also demonstrated that replacement of the paramagnetic $[Nb^{IV}(CN)_8]^{4-}$ by its diamagnetic relatives $[Mo^{IV}(CN)_8]^{4-}$ and $[W^{IV}(CN)_8]^{4-}$ in $\{[Mn^{II}(H_2O)_2]_2[Nb^{IV}(CN)_8]\cdot 4H_2O\}_n$ gives simple isostructural paramagnets.[15a] All of these studies, however, lack the systematic character that would allow identification of the factors controlling the strength and sign of magnetic coupling between various 3d metal centers and the $[Nb^{IV}(CN)_8]$ moiety. Such an analysis was performed for magnetic Prussian Blue analogues[4] and resulted in the rational design of room temperature molecular magnets.

Herein we present the preparation, structures, and magnetic properties of a series of isostructural compounds with the general formula $\{[M^{II}(\text{pyrazole})_4]_2[Nb^{IV}(CN)_8]\cdot 4H_2O\}_n$, where the paramagnetic center M^{II} is changed systematically from Mn^{II} (**1**), through HS Fe^{II} (**2**) and HS Co^{II} (**3**), to Ni^{II} (**4**). All four compounds crystallize in the same $I4_1/a$ space group and have identical structures based on cyanido bridges connecting the M^{II} and Nb^{IV} centers together. **1** and **2** are ferrimagnets with ordering temperatures T_c of 24 and 8 K, and **3** and **4** are ferromagnets with T_c values of 6 and 13 K, respectively. Specific symmetry features of the $\{[M^{II}(\text{pyrazole})_4]_2[Nb^{IV}(CN)_8]\cdot 4H_2O\}_n$ crystal lattice result in the exact geometrical equivalence of the $M^{II}-NC-Nb^{IV}$ linkages, which are the main exchange coupling pathways between the metal centers in **1**−**4**.

We also discuss the correlation between the decreasing number of unpaired electrons of the M^{II} center (5, 4, 3, and 2 for **1**−**4**, respectively) and the increasing trend in the exchange coupling constant.

Isomorphs **3** and **4** are the first known examples of $[Nb^{IV}(CN)_8]$-based molecular magnets incorporating Co^{II} and Ni^{II} centers.

2. Experimental Section

2.1. Materials. Chemicals and solvents used in this study were purchased from commercial sources (Fluka and Aldrich) and used without further purification. Potassium octacyanoniobate(IV) dihydrate, $K_4[Nb(CN)_8]\cdot 2H_2O$, was prepared according to literature procedures.[16]

2.2. Synthesis of $\{[Mn^{II}(\text{pyrazole})_4]_2[Nb^{IV}(CN)_8]\cdot 4H_2O\}_n$ (1). Aqueous solutions of $MnCl_2\cdot 4H_2O$ (4 mL, 0.10 g, 0.5 mmol) and pyrazole (4 mL, 0.30 g, 4.7 mmol) were mixed and added to the aqueous solution of $K_4[Nb(CN)_8]\cdot 2H_2O$ (7 mL, 0.05 g, 0.1 mmol). The resulting yellow solution was left in the dark at room temperature for crystallization. After 1 h, yellow single crystals of **1** were isolated from the mother liquor by repeated decantation and filtration, dried in air, and stored in a closed vessel in the dark. Yield: 15 mg (14%). Anal. Calcd for $C_{32}H_{40}Mn_2N_{24}NbO_4$: C, 37.40; H, 3.92; N, 32.71. Found: C, 37.25; H, 3.83; N, 32.63. IR (KBr, cm^{-1}): $\nu(C{\equiv}N)$ 2130 m, 2125s; $\nu(C{=}N)$ and $\nu(C{=}C)$ 1545w, 1522w, 1486vw, 1465w, 1403 m; $\delta(CH{=}CH)$ 772vs.

2.3. Synthesis of $\{[Fe^{II}(\text{pyrazole})_4]_2[Nb^{IV}(CN)_8]\cdot 4H_2O\}_n$ (2). Degassed aqueous solutions of Mohr's salt $(NH_4)_2Fe(SO_4)_2\cdot 6H_2O$ (5 mL, 0.08 g, 0.2 mmol) and pyrazole (10 mL, 0.10 g, 1.5 mmol) were mixed and added to the aqueous solution of $K_4[Nb(CN)_8]\cdot 2H_2O$ (13 mL, 0.05 g, 0.1 mmol) under an inert gas atmosphere. The resulting orange solution was left in the dark at room temperature for crystallization. After 1 h, dark-violet single crystals of **2** were isolated from the mother liquor by repeated decantation and filtration, dried in air, and stored in a closed vessel at −20 °C. Yield: 12 mg (11%). Anal. Calcd for $C_{32}Fe_2H_{40}N_{24}NbO_4$: C, 37.34; H, 3.92; N, 32.66. Found: C, 37.18; H, 3.95; N, 32.56. IR (KBr, cm^{-1}): $\nu(C{\equiv}N)$ 2130 m, 2119s; $\nu(C{=}N)$ and $\nu(C{=}C)$ 1544w, 1522w, 1490vw, 1466w, 1403 m; $\delta(CH{=}CH)$ 772vs.

2.4. Synthesis of $\{[Co^{II}(\text{pyrazole})_4]_2[Nb^{IV}(CN)_8]\cdot 4H_2O\}_n$ (3). Cold aqueous solutions of $CoCl_2\cdot 6H_2O$ (3 mL, 0.015 g, 0.07 mmol) and pyrazole (2 mL, 0.033 g, 0.5 mmol) were mixed and added dropwise to the cold aqueous solution of $K_4[Nb(CN)_8]\cdot 2H_2O$ (17 mL, 0.05 g, 0.1 mmol). The resulting light-orange solution was left in the dark at 4 °C for crystallization. After 1 h, yellow single crystals of **3** were isolated from the mother liquor by repeated decantation and filtration, dried in air, and stored in a closed vessel at room temperature. Yield: 5 mg (4%). Anal. Calcd for $C_{32}Co_2H_{40}N_{24}NbO_4$: C, 37.11; H, 3.89; N, 32.46. Found: C, 36.92; H, 3.79; N, 32.32. IR (KBr, cm^{-1}): $\nu(C{\equiv}N)$ 2131 m, 2123s; $\nu(C{=}N)$ and $\nu(C{=}C)$ 1540w, 1522w, 1488vw, 1466w, 1403 m; $\delta(CH{=}CH)$ 771vs.

2.5. Synthesis of $\{[Ni^{II}(\text{pyrazole})_4]_2[Nb^{IV}(CN)_8]\cdot 4H_2O\}_n$ (4). Aqueous solutions of $NiCl_2\cdot 6H_2O$ (10 mL, 0.05 g, 0.2 mmol) and pyrazole (5 mL, 0.10 g, 1.5 mmol) were mixed and added dropwise to the aqueous solution of $K_4[Nb(CN)_8]\cdot 2H_2O$ (14 mL, 0.05 g, 0.1 mmol). The resulting light-green suspension was left in the dark for crystallization. After 1 h, a light-green crystalline powder of **4** was isolated from the mother liquor by

---

(10) (a) Ohkoshi, S. I.; Shimura, J.; Ikeda, K.; Hashimoto, K. *J. Opt. Soc. Am. B* **2005**, *22*, 196. (b) Tsunobuchi, Y.; Kosaka, W.; Nuida, T.; Ohkoshi, S. I. *CrystEngComm* **2009**, *11*, 2051–2053. (c) Train, C.; Nuida, T.; Gheorghe, R.; Gruselle, M.; Ohkoshi, S. I. *J. Am. Chem. Soc.* **2009**, *131*, 16838–16843.

(11) (a) Rikken, G. L. J. A.; Raupach, E. *Nature* **1997**, *390*, 493. (b) Train, C.; Gheorghe, R.; Krstic, V.; Chamoreau, L.-M.; Ovanesyan, N. S.; Rikken, G. L. J. A.; Gruselle, M.; Verdaguer, M. *Nat. Mater.* **2008**, *7*, 729. (c) Inoue, K.; Imai, H.; Ghalsasi, P. S.; Kikuchi, K.; Ohba, M.; Ōkawa, H.; Yakhmi, J. V. *Angew. Chem., Int. Ed.* **2001**, *40*, 4242. (d) Coronado, E.; Galán-Mascarós, J. R.; Gómez-García, C. J.; Martínez-Ferrero, E.; Almeida, M.; Waerenborgh, J. C. *Eur. J. Inorg. Chem.* **2005**, 2064.

(12) (a) Venkatakrishnan, T. S.; Rajamani, R.; Ramasesha, S.; Sutter, J.-P. *Inorg. Chem.* **2007**, *46*, 9569–9574. (b) Pradhan, R.; Desplanches, C.; Guionneau, P.; Sutter, J.-P. *Inorg. Chem.* **2003**, *42*, 6607. (c) Venkatakrishnan, T. S.; Sahoo, Sh.; Bréfuel, N.; Duhayon, C.; Paulsen, C.; Barra, A.-L.; Ramasesha, S.; Sutter, J.-P. *J. Am. Chem. Soc.* **2010**, DOI: 10.1021/ja9089389.

(13) (a) Podgajny, R.; Pinkowicz, D.; Korzeniak, T.; Nitek, W.; Rams, M.; Sieklucka, B. *Inorg. Chem.* **2007**, *46*, 10416. (b) Pinkowicz, D.; Podgajny, R.; Nitek, W.; Makarewicz, M.; Czapla, M.; Mihalik, M.; Baanda, M.; Sieklucka, B. *Inorg. Chim. Acta* **2008**, *361*, 3957. (c) Pinkowicz, D.; Podgajny, R.; Baanda, M.; Makarewicz, M.; Gawe, B.; Łasocha, W.; Sieklucka, B. *Inorg. Chem.* **2008**, *47*, 9745. (d) Pinkowicz, D.; Podgajny, R.; Peka, R.; Nitek, W.; Baanda, M.; Makarewicz, M.; Czapla, M.; Żukrowski, J.; Kapusta, Cz.; Zając, D.; Sieklucka, B. *Dalton Trans.* **2009**, 7771–7777.

(14) (a) Kosaka, W.; Hashimoto, K.; Ohkoshi, S.-I. *Bull. Chem. Soc. Jpn.* **2008**, *81*, 992–994. (b) Arai, M.; Kosaka, W.; Matsuda, T.; Ohkoshi, S.-I. *Angew. Chem., Int. Ed.* **2008**, *47*, 6885–6887. (c) Kosaka, W.; Imoto, K.; Tsunobuchi, Y.; Ohkoshi, S.-I. *Inorg. Chem.* **2009**, *48*, 4604–4606.

(15) (a) Herrera, J. M.; Franz, P.; Podgajny, R.; Pilkington, M.; Biner, M.; Decurtins, S.; Stoeckli-Evans, H.; Neels, A.; Garde, R.; Dromzée, Y.; Julve, M.; Sieklucka, B.; Hashimoto, K.; Ohkoshi, S.-I.; Verdaguer, M. *C. R. Chimie* **2008**, *11*, 1192–1199. (b) Pilkington, M.; Decurtins, S. *Chimia* **2000**, *54*, 593.

(16) Kiernan, P. M.; Griffith, W. P. *J. Chem. Soc., Dalton Trans.* **1975**, 2489.

Table 1. Selected Crystallographic Data for the Series **1**−**4**

	1 (M = Mn)	**2** (M = Fe)	**3** (M = Co)	**4** (M = Ni)
formula	$C_{32}H_{40}Mn_2N_{24}NbO_4$	$C_{32}Fe_2H_{40}N_{24}NbO_4$	$C_{32}Co_2H_{40}N_{24}NbO_4$	$C_{32}H_{40}N_{24}NbNi_2O_4$
fw [g mol^{-1}]	1027.67	1029.49	1035.65	1035.21
cryst syst	tetragonal	tetragonal	tetragonal	tetragonal
space group	$I4_1/a$	$I4_1/a$	$I4_1/a$	$I4_1/a$
a [Å]	21.8528(4)	21.659(5)	21.5920(4)	21.4340(4)
c [Å]	9.6461(2)	9.618(5)	9.6120(2)	9.6410(2)
V [Å^3]	4606.6(2)	4512(3)	4481.3(2)	4429.2(2)
Z	4	4	4	4
cryst density d_x [g cm^{-3}]	1.482	1.516	1.535	1.552
cryst size [mm^3]	0.35 × 0.35 × 0.15	0.08 × 0.08 × 0.02	0.20 × 0.15 × 0.05	0.08 × 0.08 × 0.04
cryst color	pale yellow	dark violet	yellow	greenish yellow
data/restraints/param	3363/2/153	1910/2/150	2566/2/153	2543/2/153
R1 [$I > 2\sigma(I)$]	0.0394	0.0407	0.0358	0.0358
wR2	0.0993	0.0977	0.0688	0.0692
S	1.067	0.928	1.128	1.070

repeated decantation and filtration, dried in air, and stored in a closed vessel at −20 °C. Yield: 25 mg (24%). Anal. Calcd for $C_{32}H_{40}N_{24}NbNi_2O_4$: C, 37.13; H, 3.89; N, 32.48. Found: C, 37.08; H, 3.88; N, 32.59. IR (KBr, cm^{-1}): ν(C≡N) 2133 m, 2125s; ν(C=N) and ν(C=C) 1544w, 1524w, 1487vw, 1465w, 1405 m; δ(CH=CH) 768vs. Single crystals of **4** were obtained at 4 °C using more diluted solutions. The experimental powder X-ray diffraction (PXRD) pattern of **4** is in perfect agreement with the one calculated from single-crystal XRD data (Figure S1 in the Supporting Information).

2.6. Structure Solution and Refinement. The single-crystal XRD data for **1**, **3**, and **4** were collected at room temperature on a Nonius Kappa CCD diffractometer equipped with a Mo Kα radiation source and a graphite monochromator (λ = 0.710 73 Å). The single-crystal XRD data for **2** were collected at the same temperature on an Oxford Diffraction SuperNova CCD (Atlas) diffractometer (κ geometry) using a Mo Kα radiation source (λ = 0.710 73 Å). The space groups were determined using *ABSEN*.[17] All structures were solved by direct methods using *SIR-97*.[18] Refinement and further calculations were carried out using *SHELXL-97*.[19] The non-H atoms were refined anisotropically using weighted full-matrix least squares on F^2. H atoms joined to the C and N atoms of pyrazole ligands were positioned with an idealized geometry and refined using a riding model with U_{iso}(H) fixed at $1.2U_{eq}$(C) or $1.2U_{eq}$(N), respectively. H atoms joined to O atoms of crystallization water were found from the difference Fourier map. Structural diagrams were prepared using *Mercury 1.4.2*, *VESTA*,[20] *Ortep32*,[21] and *POV-Ray*[22] software.

2.7. Magnetic Measurements. Magnetic measurements for polycrystalline **1**, **3**, and **4** were carried out using a Lakeshore 7225 susceptometer. Magnetic measurements for **2** and an additional magnetization versus temperature measurement up to 300 K at 1 kOe for **1**, **3**, and **4** were performed using a Quantum Design MPMS5-XL SQUID magnetometer. The magnetic susceptibility data were corrected for diamagnetic contributions using Pascal's constants.[23]

2.8. Other Physical Measurements. Elemental analyses (C, H, and N) were performed using an Elementar vario MICRO cube elemental analyzer. IR spectra were measured in KBr pellets between 4000 and 400 cm^{-1} using a Bruker EQUINOX 55 FT-IR spectrometer. The PXRD pattern of **4** was recorded at room temperature on a PANalytical X'PERT PRO MPD diffractometer (Cu Kα radiation) equipped with a PSD PIXCEL detector with 0.0273° steps in the 5−50° 2θ range and a reflectionless sample holder.

Table 2. Selected Bond Lengths (Å) and Angles (deg) in the Series **1**−**4**

	1 (M = Mn)	**2** (M = Fe)	**3** (M = Co)	**4** (M = Ni)
M−N1	2.258(2)	2.198(3)	2.174(2)	2.131(2)
M−N11	2.232(2)	2.161(3)	2.115(2)	2.076(2)
M−N21	2.251(2)	2.181(3)	2.138(2)	2.106(2)
Nb−C1	2.260(2)	2.263(4)	2.264(2)	2.272(2)
Nb−C2	2.258(2)	2.253(4)	2.254(3)	2.251(3)
C1−N1	1.149(3)	1.154(5)	1.158(3)	1.155(3)
C2−N2	1.144(3)	1.134(5)	1.142(3)	1.143(3)
M−N1−C1	163.2(2)	164.2(3)	164.4(2)	164.4(2)
N1−C1−Nb	177.0(2)	175.9(3)	176.2(2)	176.3(2)
M···Nb	5.60(1)	5.55(1)	5.53(1)	5.49(1)

2.9. Calculations. Continuous shape measure (CShM) analysis for coordination spheres of M^{II} and Nb^{IV} in **1**−**4** was performed with the use of *SHAPE* software, version 1.1b.[24]

3. Results and Discussion

Crystal Structures. Single-crystal XRD revealed that compounds **1**−**4** crystallize in the same tetragonal space group $I4_1/a$ and are isomorphous. The unit cell of the $\{[M^{II}(pyrazole)_4]_2[Nb^{IV}(CN)_8]\cdot 4H_2O\}_n$ series contracts gradually on going from **1** to **4**. Table 1 shows the detailed crystallographic data for **1**−**4**, Figure S2 (Supporting Information) presents the respective asymmetric units (ASU) with atom-labeling schemes, and Table 2 lists selected bond lengths and angles.

The structures of all four isomorphs are identical and consist of a 3D cyanido-bridged M^{II}−NC−Nb^{IV} skeleton "decorated" with pyrazole molecules coordinated to 3d metal centers (Figure 1a). The cyanido skeletons of **1**−**4** comprise two sets of oppositely corrugated square grids

---

(17) McArdle, P. *J. Appl. Crystallogr.* **1996**, *29*, 306.

(18) Altomare, A.; Burla, M. C.; Camalli, M.; Cascarano, G. L.; Giacovazzo, C.; Guagliardi, A.; Moliterni, A. G. G.; Polidori, G.; Spagna, R. *J. Appl. Crystallogr.* **1999**, *32*, 115.

(19) Sheldrick, G. M. *Acta Crystallogr.* **2008**, *A64*, 112–122.

(20) Momma, K.; Izumi, F. *Comm. Crystallogr. Comput., IUCrNewslett* **2006**, *7*, 106.

(21) Farrugia, L. J. *J. Appl. Crystallogr.* **1997**, *30*, 565.

(22) Persistence of Vision Pty. Ltd. *Persistence of Vision Raytracer*, version 3.6 [computer software], 2004, retrieved from http://www.povray.org/download/.

(23) Kahn, O. *Molecular Magnetism*; VCH Publishers, Inc.: New York, 1993.

(24) (a) Llunell, M.; Casanova, D.; Cirera, J.; Bofill, J. M.; Alemany, P.; Alvarez, S.; Pinsky, M.; Avnir, D. *SHAPE v. 1.1b. Program for the Calculation of Continuous Shape Measures of Polygonal and Polyhedral Molecular Fragments*; University of Barcelona: Barcelona, Spain, 2005. (b) Casanova, D.; Cirera, J.; Llunell, M.; Alemany, P.; Avnir, D.; Alvarez, S. *J. Am. Chem. Soc.* **2004**, *126*, 1755. (c) Alvarez, S.; Alemany, P.; Casanova, D.; Cirera, J.; Llunell, M.; Avnir, D. *Coord. Chem. Rev.* **2005**, *249*, 1693. (d) Casanova, D.; Llunell, M.; Alemany, P.; Alvarez, S. *Chem.—Eur. J.* **2005**, *11*, 1479. (f) Cirera, J.; Ruiz, E.; Alvarez, S. *Chem.—Eur. J.* **2006**, *12*, 3162.

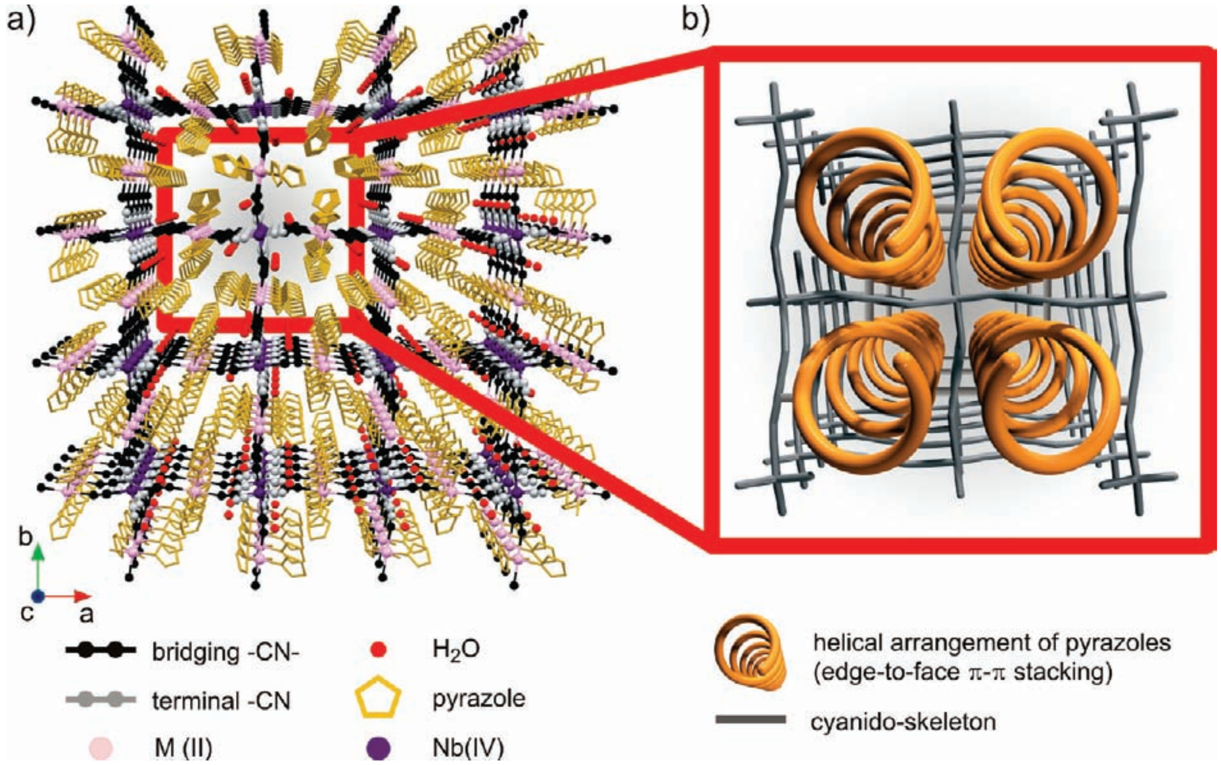

Figure 1. (a) Packing diagram of **1**−**4** along the *c* axis showing their 3D cyanido-bridged M^{II}−NC−Nb^{IV} skeleton “decorated” with pyrazole molecules. (b) Schematic representation of the helical arrangement of pyrazole ligands in the channels along the *c* axis.

interconnected in half of the Nb centers (interconnection Nb) and shifted mutually by $^1/_2a + ^1/_2b$ (Figure 2). The channels between square grids are filled with edge-to-face $\pi-\pi$-stacked pyrazole ligands adopting a helical arrangement down the *c* axis. Because of the centrosymmetry of the $I4_1/a$ space group, the handedness of the neighboring pyrazole helices is opposite (Figure 1b).

The coordination spheres of Nb^{IV} (CN = 8) in **1**−**4** comprise eight C atoms of eight cyanido ligands and in all cases adopt the geometry of a slightly distorted dodecahedron, as is indicated by the results of CShM analysis (Table 3) and the investigation of selected sets of dihedral angles δ and nonplanarity angles φ^{25} (Table S3 in the Supporting Information). Because of the fact that Nb atoms lay on the 4-fold rotoinversion axis (*c* direction), the distortion is symmetrical: C1 atoms of the bridging cyanides are slightly shifted toward the equatorial plane of the complex, and C2 atoms of the nonbridging cyanides are shifted in the opposite direction in comparison to the idealized dodecahedral (DD-8) geometry (Figure 3a). C1 and C2 atoms of the $[Nb^{IV}(CN)_8]$ moiety lie approximately in the “B-like” and “A-like” vertexes of the dodecahedron, respectively. The coordination spheres of the M^{II} centers in all four compounds adopt almost perfectly octahedral geometry (as indicated by the results of CShM analysis; Table 3 and Figure 3b) and comprise four equatorial N atoms of the pyrazole ligands (N11 and N21) and two axial N atoms of the bridging cyanido ligands (N1). The presence of four and two bridging cyanido ligands per one Nb^{IV} and one M^{II} center, respectively, gives rise to the 4:2 connectivity type, quite rare for 3D coordination systems.[13]

The metric parameters of the M^{II}−NC−Nb^{IV} linkages are almost identical in the whole series **1**−**4** (Table 2) except the M−$N1_{cyanido}$ bond length, which decreases for about 0.13 Å on going from **1** to **4** (Figure 4). A similar trend is also observed for M−$N11_{pyrazole}$ and M−$N21_{pyrazole}$ interatomic distances (shrinking up to 0.15 Å). The decrease of the M−N bond lengths in **1**−**4** is consistent with increasing ligand-field stabilization energy along the 3d metal series. Along with the shortening of the M−N1 bond length, the $M^{II}\cdots Nb^{IV}$ distance decreases from 5.60 Å for **1** to 5.55 Å for **2**, 5.53 Å for **3**, and 5.49 Å for **4**. All M^{II}−NC−Nb^{IV} linkages in the structures of **1**−**4** are symmetry-equivalent.

The 3D cyanido-bridged skeleton of **1**−**4** is stabilized by the edge-to-face $\pi-\pi$ stacking interactions between pyrazole ligands arranged in helical superstructures running along the 4-fold screw axis (Figure S4 in the Supporting Information) in the channels formed by the cyanido skeleton down the *c* direction (Figure 1b) with the shortest distances of 3.381, 3.387, 3.395, and 3.392 Å for **1**−**4**, respectively. Additional stabilization is completed by hydrogen bonds between the pyrazole ligands, terminal cyanides, and water of crystallization.

IR Spectra. IR spectra of the series **1**−**4** (Figure S5 in the Supporting Information) are very similar with small systematic shifts in the 2200−2000 cm^{-1} region, where bands characteristic for the stretching vibrations of cyanido ligands occur. In each case, the presence of two peaks in this region indicates the bridging (higher frequency) and terminal (lower frequency) functions of CN groups. In the **2**−**4** row, the frequencies increase from 2130 and 2119 cm^{-1} for **2**, through 2131 and 2123 cm^{-1} for **3**, to 2133 and 2125 cm^{-1} for **4** along with a decrease of the M−N1 bond lengths. These changes are caused mainly by

---

[25] Muetterties, E. L.; Guggenberger, L. J. *J. Am. Chem. Soc.* **1974**, *96*, 1748–1756.

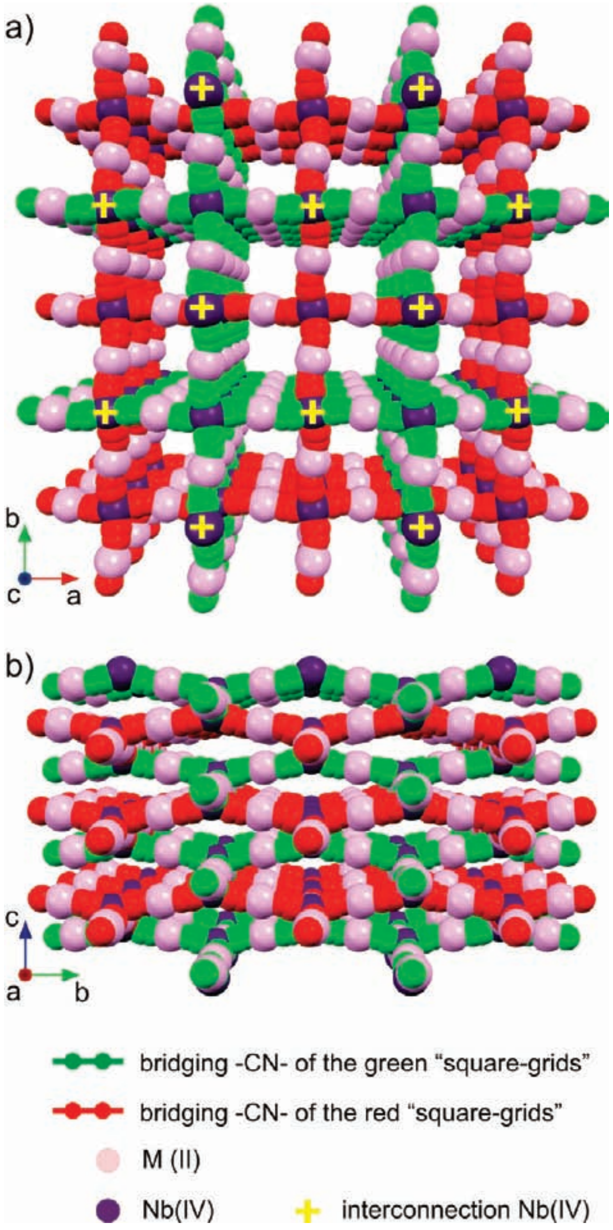

Figure 2. Packing diagrams of the structures **1**−**4** along the *c* (a) and *a* (b) directions, showing their cyanido skeletons comprising two sets of oppositely corrugated square grids shifted mutually by $^1/_2a + {}^1/_2b$.

the electron-density withdrawal from the sp σ^* molecular orbital of the CN ligands by metal centers and kinematic coupling in the $M^{II}-NC-Nb^{IV}$ unit. This tendency is not observed for **1** with peaks at 2130 and 2125 cm^{-1}, probably because of the much longer M−N1 bonds.

IR spectra of **1**−**4** also show peaks due to the presence of water of crystallization [ν(OH) and γ(OH) around 3600 and 1600 cm^{-1}, respectively] and pyrazole ligands [ν(NH) around 3400 cm^{-1}, ν(CH) between 3100 and 2700 cm^{-1}, and ring-deformation vibrations in the fingerprint region].

Magnetic Properties. To estimate the values of the exchange coupling constants J_{M-Nb}, we have analyzed the magnetization versus temperature curves for **1**−**4** using the molecular field model.[26] Because the magnetic centers in **1**−**4** are linked by one type of symmetry-equivalent $Nb^{IV}-C1N1-M^{II}$ linkage, only a single exchange coupling J_{M-Nb} is assumed. The molecular field model consists of two sublattices: one for the Nb^{IV} center and one for the M^{II} center. Only the superexchange coupling between the nearest neighbors is taken into account. The main ingredient of the model is a set of coupled equations for the thermally averaged values of sublattice spins:

$$\langle S_M\rangle = S_{M0}B_{S_{M0}}\left(\frac{g_M\mu_B S_{M0}H_0}{k_BT} + \frac{Z_{M-Nb}J_{M-Nb}S_{M0}}{k_BT}\langle S_{Nb}\rangle\right) \qquad (1)$$

$$\langle S_{Nb}\rangle = S_{Nb0}B_{S_{Nb0}}\left(\frac{g_{Nb}\mu_B S_{Nb0}H_0}{k_BT} + \frac{Z_{Nb-M}J_{M-Nb}S_{Nb0}}{k_BT}\langle S_M\rangle\right) \qquad (2)$$

where B_S is the Brillouin function, S_{M0} and S_{Nb0} are the values of $\langle S_M\rangle$ and $\langle S_{Nb}\rangle$ at T = 0 K, H_0 is the external magnetic field, g_M and g_{Nb} are the spectroscopic *g* factors of the M^{II} and Nb^{IV} centers, respectively, Z_{ij} are the numbers of the nearest-neighbor *j*-site centers surrounding an *i*-site center, k_B is the Boltzmann constant, and μ_B is the Bohr magneton. The mean values $\langle S_M\rangle$ and $\langle S_{Nb}\rangle$ are calculated by numerically iterating these equations, and the total molar magnetization is obtained as

$$M_{total} = N_A\mu_B[\lambda g_M\langle S_M\rangle + \mu g_{Nb}\langle S_{Nb}\rangle] \qquad (3)$$

where μ and λ represent the mole fractions of the Nb^{IV} and M^{II} centers, respectively, and $\langle S_M\rangle$ and $\langle S_{Nb}\rangle$ will differ in sign for antiferromagnetic coupling.

Because compounds **1**−**4** are isostructural, the numbers of nearest neighbors $Z_{M-Nb} = 2$ and $Z_{Nb-M} = 4$ and the molar fractions $\mu = 1$ and $\lambda = 2$ are the same in all cases. Additionally, for **1**−**4**, we assume $S_{Nb0} = {}^1/_2$ and an isotropic *g* factor g_{Nb} = 2.0.[16] The spin quantum number S_{M0} of the M^{II} centers and the corresponding spectroscopic *g* factors g_M are case-dependent.

All calculated molecular field curves for **1**−**4** display higher values of magnetization at low temperature because of the fact that molecular field theory does not account for the complex magnetizing process. Consequently, the agreement between the model and experimental curves is poor. However, in each case, the corresponding peak of the model d*M*/d*T* coincides well with the one obtained from experimental data. Hence, the estimation of the J_{M-Nb} values in all four cases is reasonably accurate.

In the high-temperature range (much above T_c), the molecular field prediction for the magnetic susceptibility reads

$$\chi = \frac{(2C_{S_{M0}} + C_{S_{Nb0}})T + 4\lambda_{M-Nb}C_{S_{M0}}C_{S_{Nb0}}}{T^2 - 2\lambda_{M-Nb}{}^2C_{S_{M0}}C_{S_{Nb0}}} \qquad (4)$$

where $C_S = N_Ag^2\mu_B{}^2S(S+1)/3k_B$ denotes the Curie constant for the corresponding spins of M^{II} and Nb^{IV} and λ_{M-Nb} is the molecular field constant. This high-temperature

---

(26) Ohkoshi, S.-I.; Iyoda, T.; Fujishima, A.; Hashimoto, K. *Phys. Rev. B* **1997**, *56*, 11642–11652.

Table 3. CShM Analysis[a] Results for the Coordination Spheres of Nb^{IV} Centers in **1**−**4**

	DD[b]	SAPR[c]	JBTP[d]	**1**	**2**	**3**	**4**
S_{DD}	ca. 2.8	0	ca. 3.4	0.221	0.215	0.195	0.200
S_{SAPR}	0	ca. 2.8	ca. 2.8	2.967	2.966	2.951	2.957
S_{JBTP}	ca. 3.4	ca. 2.8	0	3.234	3.260	3.257	3.297
$\Delta_{DD\text{-}SAPR}$	0	0		0.30	0.29	0.28	0.28
$\varphi_{SAPR\to DD}$	100%	0%		102%	102%	102%	102%
$\varphi_{DD\to SAPR}$	0%	100%		28%	27%	26%	26%
$\Delta_{DD\text{-}JBTP}$	0		0	0.24	0.24	0.22	0.23
$\varphi_{JBTP\to DD}$	100%		0%	98%	98%	98%	99%
$\varphi_{DD\to JBTP}$	0%		100%	26%	25%	24%	24%
judgment				DD slightly distorted toward JBTP and SAPR			

[a] S_{DD}, S_{SAPR}, S_{JBTP} = shape measures relative to DD, SAPR, and JBTP, respectively; $\Delta_{DD\text{-}SAPR}$ and $\Delta_{DD\text{-}JBTP}$ represent deviation from the DD-SAPR and DD-JBTP interconversion paths, respectively; $\varphi_{A\to B}$ = angular path fractions; equal to 0 when the real geometry coincides with A and equal to 100 for B. [b] Triangular dodecahedron. [c] Square antiprism. [d] Johnson's bicapped trigonal prism.

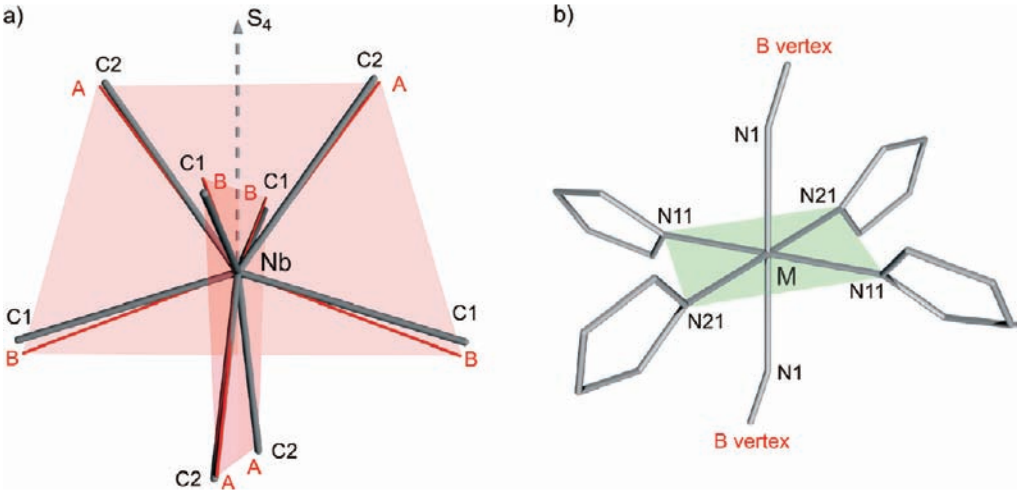

Figure 3. (a) Geometry of the $[Nb^{IV}(CN)_8]$ moiety in **1** (gray sticks) and its idealized dodecahedral geometry obtained from CShM analysis (red sticks). Bridging cyanides on the "B-like" vertexes of DD and terminal cyanides on the "A-like" vertexes (for **2**−**4**, the geometries of $[Nb^{IV}(CN)_8]^{4-}$ are identical). (b) Geometry of the coordination sphere of Mn^{II} centers (for **2**−**4**, the geometries of M^{II} are identical).

law is a counterpart of the Curie−Weiss law for unequal occupation numbers of the constituent magnetic sublattices. The positive (negative) sign of the molecular field constant corresponds to the (anti)ferromagnetic character of the magnetic coupling.

Magnetic Properties of 1. The temperature dependence of magnetization $M(T)$ for **1** measured at 0.5 kOe (points) is presented in Figure 5a. On cooling down, the M values increase slowly, and then the signals rise up abruptly, reaching the highest rate point at about 23.8 K (cf. the inset in Figure 5a), and saturate at low temperatures. Such behavior suggests the presence of a long-range magnetic order below critical temperature $T_c = 23.8$ K (determined as the position of the dM/dT peak). The magnetization versus field plot measured at $T = 4.3$ K (Figure 5b) increases rapidly and reaches the saturation value of 8.95 μ_B at 56 kOe, which is very close to that expected for antiferromagnetic coupling between Mn^{II} and Nb^{IV} sublattices: $2g_{Mn}S_{Mn0} - g_{Nb}S_{Nb0} = 9\ \mu_B$, assuming $g_{Mn} = 2.0$ and $S_{Mn0} = {}^5/_2$. The observed magnetic hysteresis loop is extremely narrow ($H_c \approx 10$ Oe).

The calculated molecular field $M(T)$ curve in the 4−50 K range (Figure 5a, solid line) assuming an antiferromagnetic interaction between Mn^{II} and Nb^{IV} sublattices gives $J_{Mn-Nb} = -6.8(2)\ cm^{-1}$. The molecular field curve has been chosen so that the corresponding peak of dM/dT coincides with that obtained from experimental data (inset in Figure 5a). The error of J_{M-Nb} was estimated assuming the uncertainty of 0.5 K in the peak position.

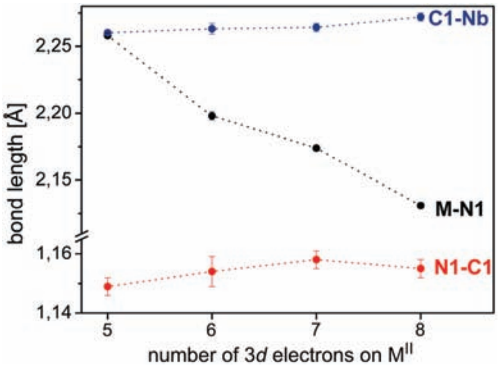

Figure 4. Variation of the C1−Nb (blue), M−N1 (black), and N1−C1 (red) bond lengths in the series **1**−**4** showing significant gradual reduction of the M−N1 distance in the **1**−**4** row (dotted lines are guides for the eye).

The inset in Figure 5b shows the temperature variation of the inverse susceptibility for **1** (points). The fit to the molecular field prediction in the 240−300 K range (solid line) yielded $\lambda_{Mn-Nb} = -28(4)$ mol cm^{-3} and $g_{Mn} = 1.99(1)$, which corroborate the assumption of antiferromagnetic coupling between Mn^{II} and Nb^{IV} and the value of g_{Mn}.

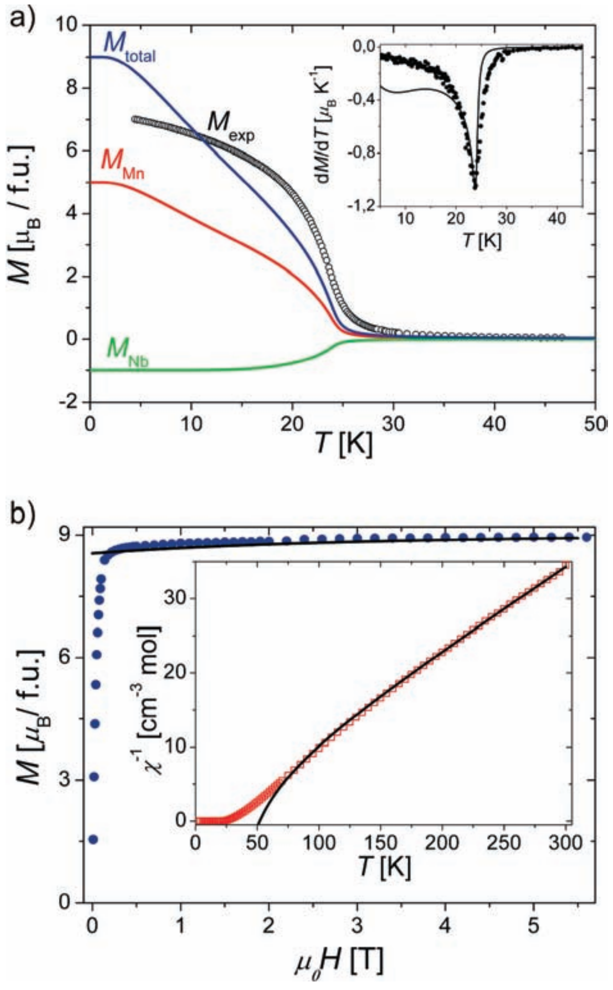

Figure 5. (a) Temperature dependence of magnetization for **1** (at H = 0.5 kOe). The solid lines are the result of molecular field calculations for two types of sites occupied by antiferromagnetically coupled Mn^{II} and Nb^{IV} ions. Inset: Corresponding derivative dM/dT used to pinpoint the value of the exchange coupling J_{Mn-Nb}. (b) Isothermal magnetization of **1** at T = 4.3 K (blue points) and its molecular field fit (black solid line). The saturation value indicates an antiferromagnetic coupling between the Mn^{II} and Nb^{IV} sublattices. Inset: Thermal dependence of the inverse susceptibility for **1** and the fit to the high-temperature molecular field prediction (solid line).

The zero-field-cooled (ZFC) and field-cooled (FC) magnetizations at H = 200 Oe (Figure S6a in the Supporting Information), together with the magnetic susceptibility measured in the alternating-current (AC) mode (f = 125 Hz and H_{ac} = 5 Oe; Figure S6b in the Supporting Information), demonstrate very sharp anomalies at 24 K for **1**, confirming magnetic ordering at this temperature.

Magnetic Properties of 2. The temperature dependence of magnetization $M(T)$ for **2** measured at 0.5 kOe (points) is presented in Figure 6a. Upon cooling, the M values increase slowly, and then the signals rise up abruptly, reaching the highest rate point at about 8.3 K (cf. the inset in Figure 6a), and saturate at low temperatures. Such behavior suggests the presence of long-range magnetic order below critical temperature T_c = 8.3 K (determined as the position of the dM/dT peak). The magnetization versus field plot measured at T = 2 K (Figure 6b) up to 1.5 kOe shows a rapid increase, followed by linear growth in higher fields. At 50 kOe, the magnetization attains the value of 7 μ_B, which is substantially lower than that expected for the ferromagnetic coupling between the Fe^{II} and Nb^{IV} ions ($2g_{Fe}S_{Fe0} + g_{Nb}S_{Nb0}$ = 9.6 μ_B) and close to that for the antiferromagnetic coupling ($2g_{Fe}S_{Fe0} - g_{Nb}S_{Nb0}$ = 7.6 μ_B), assuming g_{Fe} = 2.16[14b] and S_{Fe0} = 2. The deviation of the measured magnetization values from those obtained within the molecular field model may be due to the local anisotropy of the Fe^{II} ions and/or noncolinearity of the constituent spins. The presence of anisotropy is further implied by the substantial value of χ'' (Figure S7b in the Supporting Information). The observed magnetic hysteresis loop is very narrow with coercive field H_c = 28 Oe.

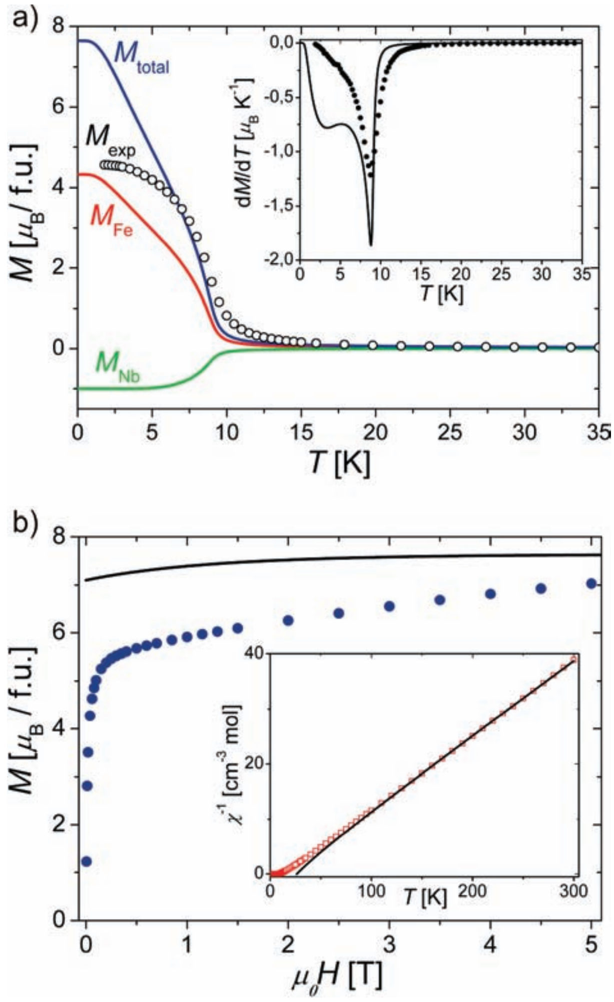

Figure 6. (a) Temperature dependence of magnetization for **2** (at H = 0.5 kOe). The solid lines are the result of molecular field calculations for two types of sites occupied by antiferromagnetically coupled Fe^{II} and Nb^{IV} ions. Inset: Corresponding derivative dM/dT used to pinpoint the value of the exchange coupling J_{Fe-Nb}. (b) Isothermal magnetization of **2** at T = 2 K (blue points) and its molecular field fit (black solid line). The saturation value indicates an antiferromagnetic coupling between the Fe^{II} and Nb^{IV} sublattices; the shape of the measured curve implies noncolinearity of the magnetic moments. Inset: thermal dependence of the inverse susceptibility for **2** and the fit to the high-temperature molecular field prediction (solid line).

The calculated molecular field $M(T)$ curve in the 2−35 K range (Figure 6a solid line) assuming an antiferromagnetic interaction between Fe^{II} and Nb^{IV} sublattices gives $J_{Fe-Nb} = -3.1(2)$ cm^{-1}. The molecular field curve has been chosen so that the corresponding peak of dM/dT coincides with that obtained from experimental data (inset in Figure 6a). The error of $J_{\mathrm{M-Nb}}$ was estimated assuming the uncertainty of 0.5 K in the peak position.

The inset in Figure 6b shows the temperature variation of the inverse susceptibility for **2** (points). The fit to the molecular field prediction in the 150−300 K range (solid line) yielded g_{Fe} = 2.163(2), which corroborates the above-mentioned assumption of the value of g_{Fe}. The value of $\lambda_{\mathrm{Fe-Nb}} = +16.2(3)$ mol cm^{-3} suggests, however, a very weak ferromagnetic interaction. This is in direct contrast with conclusions based on a more reliable analysis of the magnetization versus field curve, and therefore we assume antiferromagnetic interactions in **2**.

The ZFC and FC magnetizations at H = 50 Oe (Figure S7a in the Supporting Information), together with the magnetic susceptibility measured in the ac mode (frequency 10, 100, and 1000 Hz, H_{ac} = 3 Oe, and H_{dc} = 50 Oe; Figure S7b in the Supporting Information), demonstrate significant anomalies at 8 K for **2**, confirming magnetic ordering at this temperature.

Magnetic Properties of 3. Figure 7b shows the isothermal magnetization measured at T = 4.3 K. Up to 0.4 kOe, it shows a rapid increase, followed by a steady growth in higher fields. At 50 kOe, the magnetization attains a value of 5.55 μ_{B}, which indicates that Co$^{\mathrm{II}}$ 3d^7 is in a HS state $(t_{2g})^5(e_g)^2$. In such a case, the orbital contribution to the magnetic moment may not be neglected,[27] and special treatment is necessary. In the octahedral ligand field, the orbital degeneracy of the corresponding ground term ^{4}F (L = 3, S = $^3/_2$) is partially lifted and the term splits into two orbital triplets $\Gamma_4(^4T_{1g})$ and $\Gamma_5\ (^4T_{2g})$, and an orbital singlet $\Gamma_2(^4A_{2g})$.[28] The lowest-lying triplet G_4 behaves analogously to the state with an effective orbital angular moment $\tilde{l}$ = 1 and a negative effective $\tilde{g}_l$ factor with the expected value of $-^3/_2$ if we neglect the covalent bonding contribution. Besides the orbital degeneracy of this state, there is a 4-fold spin degeneracy corresponding to the spin quantum number S = $^3/_2$. In turn, because of the spin−orbit coupling, this orbital triplet ($\tilde{l}$ = 1) with S = $^3/_2$ splits into a lowest-lying doublet, a quartet, and a sextet with an effective total angular momentum $\tilde{j}$ equal to $^1/_2$, $^3/_2$, and $^5/_2$, respectively. At low temperature, only the lowest doublet is populated and the Co$^{\mathrm{II}}$ ion can be described by an effective spin $\tilde{S}_{\mathrm{Co}}$ = $^1/_2$, satisfying operator equations

$$\tilde{g}_l \tilde{\mathbf{l}} + g_S \mathbf{S} = g_{\mathrm{Co}} \tilde{\mathbf{S}}_{\mathrm{Co}} \tag{5}$$

and

$$\tilde{\mathbf{l}} + \mathbf{S} = \tilde{\mathbf{S}}_{\mathrm{Co}} \tag{6}$$

The effective spectroscopic factor of this doublet is given by the formula

$$g_{\mathrm{Co}} = \frac{1}{2}(\tilde{g}_l + g_S) + \frac{\tilde{l}(\tilde{l}+1) - S(S+1)}{2\tilde{S}_{\mathrm{Co}}(\tilde{S}_{\mathrm{Co}}+1)}(\tilde{g}_l - g_S) \tag{7}$$

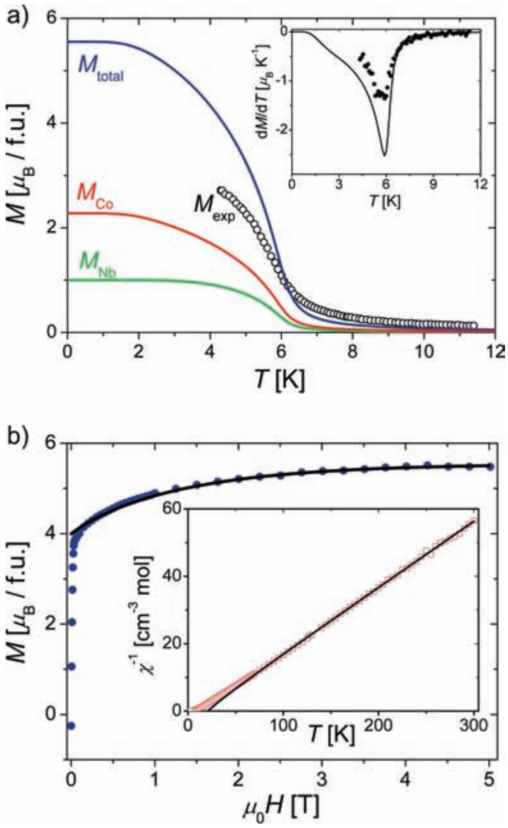

Figure 7. (a) Temperature dependence of magnetization for **3** (at H = 0.5 kOe). The solid lines are the result of molecular field calculations for two types of sites occupied by ferromagnetically coupled Co$^{\mathrm{II}}$ and Nb$^{\mathrm{IV}}$ ions. Inset: Corresponding derivative dM/dT used to pinpoint the value of the exchange coupling $J_{\mathrm{Co-Nb}}$. (b) Isothermal magnetization of **3** at T = 4.3 K (blue points) and its molecular field fit (black solid line), which was used to adjust the value of the effective spectroscopic factor g_{Co} of the lowest-lying doublet. The value at 50 kOe indicates ferromagnetic coupling between the Co$^{\mathrm{II}}$ and Nb$^{\mathrm{IV}}$ sublattices. Inset: Thermal dependence of the inverse susceptibility for **3** and the fit to the high-temperature molecular field prediction mean-field law (solid line).

The theoretically predicted value of g_{Co} is hence $^{13}/_3 \approx$ 4.33. Equations 5 and 6 determine the right form of the exchange coupling term. Projecting the genuine spin operator $\boldsymbol{S}$ of the Co$^{\mathrm{II}}$ ion onto the effective spin $\tilde{S}_{\mathrm{Co}}$, one obtains

$$\mathbf{S} = (g_{\mathrm{Co}} - \tilde{g}_l)/(g_S - \tilde{g}_l)\tilde{\mathbf{S}}_{\mathrm{Co}} \tag{8}$$

Using eq 7, it is easy to check that the prefactor in eq 8 depends only on quantum numbers $\tilde{l}$, S, and $\tilde{S}_{\mathrm{Co}}$ and is equal to $^5/_3$. Assuming an isotropic exchange coupling between the spin of Co$^{\mathrm{II}}$ and the spin of Nb$^{\mathrm{IV}}$ (this necessary simplifying assumption is due to the lack of single-crystal magnetic data), we finally obtain the proper coupling term

$$J_{\mathrm{Co-Nb}} \mathbf{S} \cdot \mathbf{S}_{\mathrm{Nb}} = \frac{5}{3} J_{\mathrm{Co-Nb}} \tilde{\mathbf{S}}_{\mathrm{Co}} \cdot \mathbf{S}_{\mathrm{Nb}} \tag{9}$$

The value of 5.55 μ_{B} attained in the field of 50 kOe (Figure 7b) is substantially larger than the value expected for the antiferromagnetic coupling between the Co$^{\mathrm{II}}$ and Nb$^{\mathrm{IV}}$ centers ($2g_{\mathrm{Co}}\tilde{S}_{\mathrm{Co}} - g_{\mathrm{Nb}}S_{\mathrm{Nb}} \approx 3.33$), and it compares well with that for the ferromagnetic coupling ($2g_{\mathrm{Co}}\tilde{S}_{\mathrm{Co}} - g_{\mathrm{Nb}}S_{\mathrm{Nb}} \approx 5.33$), assuming g_{Co} = 4.33 and $\tilde{S}_{\mathrm{Co}}$ = $^1/_2$. The observed magnetic hysteresis loop is very narrow with coercive field $H_{\mathrm{c}} \approx$ 80 Oe.

---

[27] (a) Kettle, S. F. A. *Physical Inorganic Chemistry. A Coordination Chemistry Approach*; Oxford University Press: Oxford, U.K., 1996. (b) Palii, A.; Tsukerblat, B.; Clemente-Juan, J. M.; Coronado, E. *Int. Rev. Phys. Chem.* **2010**, *29*, 135–230.

[28] Abragam, A.; Bleaney, B. *Electron Paramagnetic Resonance of Transition Ions*; Clarendon Press: Oxford, U.K., 1970.

The temperature dependence of magnetization $M(T)$ for **3** measured at 0.5 kOe (points) is presented in Figure 7a. Upon cooling, the M values increase slowly, and then the signals rise up abruptly, reaching the highest rate point at about 5.9 K (cf. the inset in Figure 7a), and saturate at low temperatures. Such behavior suggests the presence of a long-range magnetic order below critical temperature T_c = 5.9 K (determined as the position of the dM/dT peak).

The calculated molecular field $M(T)$ curve in the 4−12 K range (Figure 7a, solid line), assuming a ferromagnetic interaction between Co^{II} and Nb^{IV} sublattices, gives J_{Co-Nb} = +3.5(3) cm^{-1}. The molecular field curve has been chosen so that the corresponding peak of dM/dT coincides with that obtained from experimental data (inset in Figure 7a). The error of J_{M-Nb} was estimated assuming the uncertainty of 0.5 K in the peak position.

The inset in Figure 7b shows the temperature variation of the inverse susceptibility for **3** (points). The fit to the molecular field prediction in the 150−300 K range, assuming the effective spin $^1/_2$ for the Co^{II} centers (solid line), yielded λ_{Co-Nb} = +15(1) mol cm^{-3} and g_{Co} = 5.03(2), which corroborate a ferromagnetic interaction between the Co^{II} and Nb^{IV} sublattices. The enhanced value of the spectroscopic factor may be due to the non-negligible contribution from the excited-state levels.

The ZFC and FC magnetizations at H = 46 Oe (Figure S8a in the Supporting Information), together with the magnetic susceptibility measured in the ac mode (frequency 40, 360, and 2000 Hz and H_{AC} = 3 Oe; Figure S8b in the Supporting Information), demonstrate significant anomalies at 6 K for **3**, confirming magnetic ordering at this temperature.

Magnetic Properties of 4. For the Ni^{II} 3d^8 ion placed in the octahedral ligand field, the orbital degeneracy of the corresponding ground term ^{3}F (L = 3, S = 1) is partially lifted and the term splits into two orbital triplets $\Gamma_4(^3T_{1g})$ and $\Gamma_5(^3T_{2g})$ and a singlet $\Gamma_2(^3A_{2g})$,[27a,28] of which the orbital singlet is the lowest-lying level. Because of the spin−orbit interaction, which couples the ground orbital singlet with the triplet Γ_5, one can expect an enhancement of the mean spectroscopic factor for the Ni^{II} center ($g = g_S - 8\lambda/\Delta$, where λ is the spin−orbit coupling constant, negative for configuration 3d^8 and Δ is energy difference between the triplet and singlet). Hence, the quantum state of Ni^{II} is described by spin quantum number S_{Ni0} = 1 and the expected value of the spectroscopic factor $g_{Ni} > 2.0$.

The temperature dependence of magnetization $M(T)$ for **4** measured at 0.5 kOe (points) is presented in Figure 8a. Upon cooling, the M values increase slowly, and then the signals rise up abruptly, reaching the highest rate point at about 13.4 K (cf. the inset in Figure 8a), and saturate at low temperatures. Such behavior suggests the presence of a long-range magnetic order below critical temperature T_c = 13.4 K (determined as the position of the dM/dT peak). The magnetization versus field plot measured at T = 4.3 K (Figure 8b) shows relatively rapid saturation and attains 5.31 μ_B at 56 kOe. This value is very close to that expected for ferromagnetic coupling between Ni^{II} and Nb^{IV} sublattices: $2g_{Ni}S_{Ni0} + g_{Nb}S_{Nb0}$ = 5.36 μ_B, assuming g_{Ni} = 2.18 and S_{Ni0} = 1. The observed magnetic hysteresis loop is extremely narrow, with coercive field $H_c \approx$ 10 Oe.

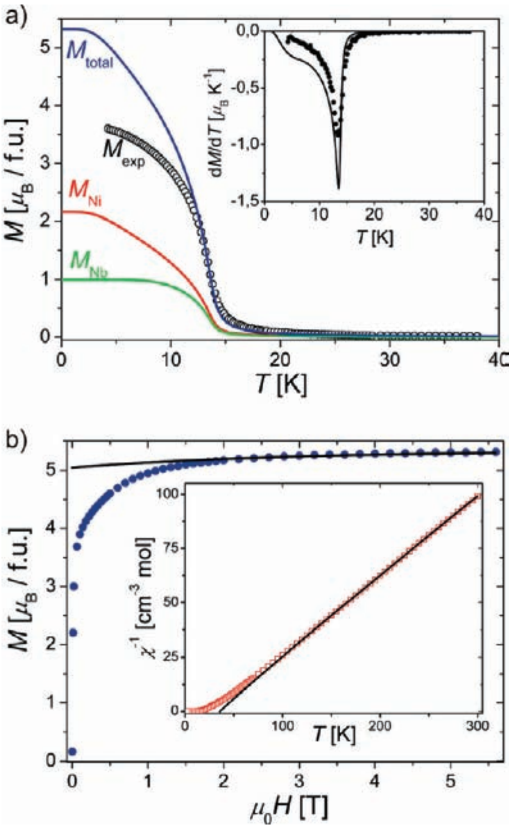

Figure 8. (a) Temperature dependence of magnetization for **4** (at H = 0.5 kOe). The solid lines are the result of molecular field calculations for two types of sites occupied by ferromagnetically coupled Ni^{II} and Nb^{IV} ions. Inset: Corresponding derivative dM/dT used to pinpoint the value of the exchange coupling J_{Mn-Nb}. (b) Isothermal magnetization of **4** at T = 4.25 K (blue points) and its molecular field fit (black solid line). The saturation value indicates ferromagnetic coupling between the Ni^{II} and Nb^{IV} sublattices. Inset: Thermal dependence of the inverse susceptibility for **4** and the fit to the high-temperature molecular field prediction (solid line).

The calculated molecular field $M(T)$ curve in the 4−40 K range (Figure 8a, solid line), assuming the ferromagnetic interaction between Ni^{II} and Nb^{IV} sublattices, gives J_{Ni-Nb} = +8.1(3) cm^{-1}. The molecular field curve has been chosen so that the corresponding peak of dM/dT coincides with that obtained from experimental data (inset in Figure 8a). The error of J_{M-Nb} was estimated assuming the uncertainty of 0.5 K in the peak position.

The inset in Figure 8b shows the temperature variation of the inverse susceptibility for **4** (points). The fit to the molecular field prediction in the 150−300 K range (solid line) yielded λ_{Ni-Nb} = +38.0(1) mol cm^{-3} and g_{Ni} = 2.180(1), which corroborate the above assumption of ferromagnetic coupling between Ni^{II} and Nb^{IV} and the value of g_{Ni}.

The ZFC and FC magnetizations at H = 50 Oe (Figure S9a in the Supporting Information), together with the magnetic susceptibility measured in the ac mode (frequency 100 and 1000 Hz and H_{ac} = 3 Oe; Figure S9b in the Supporting Information), demonstrate very sharp anomalies at 13 K for **4**, confirming magnetic ordering at this temperature. The negative values of the exchange couplings J_{M-Nb} found for **1** and **2** indicate the presence of antiferromagnetic pathways within the Nb^{IV}−CN−M^{II} linkage. They arise from the "through-bond" interaction, i.e., the overlap between the magnetic orbital centered on the 4d$_{x^2-y^2}$ orbital of the Nb^{IV} center (the lowest-lying d orbital for the dodecahedral geometry) and some of the 3d orbitals of the M^{II} center. Furthermore, the monotonic increase of exchange constants $J_{Mn-Nb} < J_{Fe-Nb} < 0 < J_{Co-Nb} < J_{Ni-Nb}$ points out that the ferromagnetic terms, which arise from the orthogonality of the Nb $4d_{x^2-y^2}$ orbital with some M^{II} 3d orbitals and contribute to the total exchange constant, may not be negligible (despite the quite large $Nb^{IV}\cdots M^{II}$ distance of about 5 Å). There is an evident correlation between the decreasing number of unpaired electrons on the M^{II} center (5, 4, 3, and 2 for **1**−**4**, respectively) and the increasing trend in the exchange coupling constant. For the DD geometry, the $d_{x^2-y^2}$ orbital of Nb^{IV} is σ-nonbonding because all C atoms of the CN ligands are located in its nodal planes.[27] On the other hand, the lowest $d_{x^2-y^2}$ level mixes substantially with the π system of the cyanido ligands. It was also shown[29] that the overlap between the $d_{x^2-y^2}$ orbital of Nb^{IV} and the π orbital of CN^- is more efficient in the "B-like" vertexes of the dodecahedral coordination sphere than in the "A-like" vertexes.[29,30] For all of the compounds **1**−**4**, the bridging cyanido ligands are located in the "B-like" vertexes, and one can expect relatively strong exchange couplings.

Among the magnetic orbitals of the M^{II} centers, two of the t_{2g} type (d_{xy} and d_{xz}) can be expected to be effectively delocalized on the N and C atoms of the bridging cyanide (π symmetry) because of the favorable $M^{II}-NC-Nb^{IV}$ linkage geometry. The corresponding superexchange pathways are shown in Figure 9a. For the remaining t_{2g} orbital (d_{yz}), a weak overlap with the orbitals of the cyanido bridge can be expected because of the moderate $M^{II}-N-C$ bending angle (Figure 9b). At the same time, the $4d_{x^2-y^2}$ magnetic orbital of Nb^{IV} is also partially delocalized on the C and N atoms of the cyanido ligand (with the same π symmetry). For two electrons, we can apply Kahn's model ($J = 2k + 4\beta S$), which predicts two competing contributions to the resulting exchange coupling. The first contribution corresponding to the exchange integral k (>0) is of ferromagnetic character, whereas the second contribution, proportional to the resonance integral β (<0) and to the overlap integral S, is antiferromagnetic. This model provides an argument for a sizable antiferromagnetic interaction for the d_{xy} and d_{xz} orbitals ($2k \ll |4\beta S|$) and a weak antiferromagnetic interaction for the remaining d_{yz} orbital ($2k < |4\beta S|$). Denoting the corresponding contributions to the total exchange coupling by J_{11}, J_{12}, and J_{13}, one can write $J_{11} < J_{12} < J_{13} < 0$. The d_{z^2} and $d_{x^2-y^2}$ orbitals (e_g orbitals) of the M^{II} ion have zero overlap integrals and result in the ferromagnetic contributions J_{14}, $J_{15} > 0$ to the total exchange coupling (Figure 9c). The total exchange integral in the $Nb^{IV}-CN-M^{II}$ unit can be expressed by the well-known formula

$$J = \frac{1}{n_A n_B}\sum_{\mu=1}^{n_A}\sum_{\nu=1}^{n_B} J_{\mu\nu} \tag{10}$$

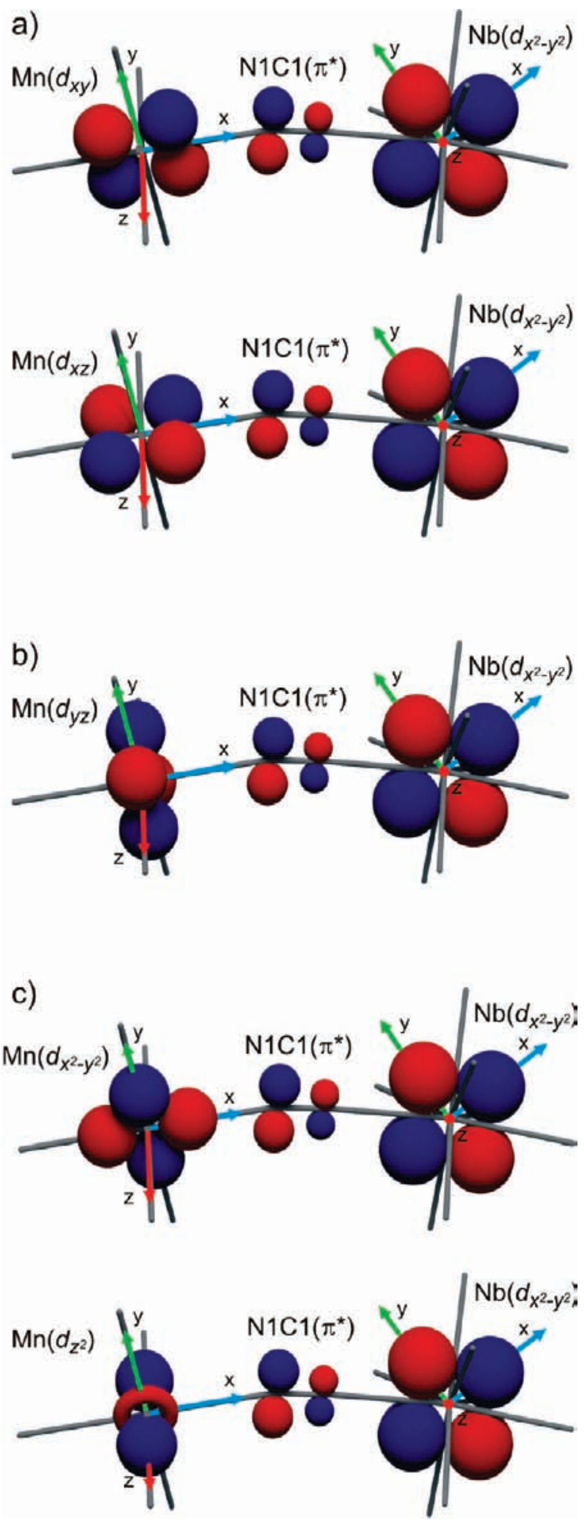

Figure 9. Strong antiferromagnetic superexchange pathways J_{11} and J_{12} (a), weak antiferromagnetic superexchange pathway J_{13} (b), and ferromagnetic superexchange pathways J_{14} and J_{15} (c).

In the formula (10), the A site corresponds to Nb^{IV} and the B site to M^{II}. Because there is only one electron on the $4d_{x^2-y^2}$ orbital of the Nb^{IV} center, we always have $n_A = n_{Nb} = 1$. The situation is case-dependent for the M^{II} center. For **1**, the electronic configuration of Mn^{II} is $(t_{2g})^3(e_g)^2$. There are five singly occupied orbitals ($n_B = n_{Mn} = 5$) and, therefore, for J_{Mn-Nb}, we obtain $J_{Mn-Nb} = {}^1/_5(J_{11} + J_{12} + J_{13} + J_{14} + J_{15})$. This expression is not sufficient to estimate

---

(29) Burdett, J. K.; Hoffmann, R.; Fay, R. C. *Inorg. Chem.* **1978**, *17*, 2553–2568.

(30) Visinescu, D.; Desplanches, C.; Imaz, I.; Bahers, V.; Pradhan, R.; Villamena, F. A.; Guionneau, P.; Sutter, J.-P. *J. Am. Chem. Soc.* **2006**, *128*, 10202–10212.

the contributions from the individual pathways, and we need to introduce the corresponding averaged contributions: average antiferromagnetic J_{AF} for each singly occupied t_{2g} orbital (replacing each individual AF contribution J_{11}, J_{12}, and J_{13}) and average ferromagnetic J_F for each singly occupied e_g orbital (replacing each individual F contribution J_{14} and J_{15}). Therefore, the expression for J_{Mn-Nb} can be written as $J_{Mn-Nb} = {}^1/_5(3J_{AF} + 2J_F)$. The same formula can be applied for the remaining compounds. For **2** with M = Fe, the electronic configuration is $(t_{2g})^4(e_g)^2$, which implies $n_B = n_{Fe} = 4$. Hence, the expression for the exchange coupling constant has the following form: $J_{Fe-Nb} = {}^1/_4(2J_{AF} + 2J_F)$. At this point, it is possible to calculate the values of both averaged contributions J_{AF} and J_F using the experimental values of $J_{Mn-Nb} = -6.8$ cm^{-1} and $J_{Fe-Nb} = -3.1$ cm^{-1} obtained from the magnetic data for **1** and **2**. The estimated values are as follows: $J_{AF} = -21.6$ cm^{-1} and $J_F = +15.4$ cm^{-1}.

The electronic configuration of the Co^{II} ion in **3** is $(t_{2g})^5(e_g)^2$, in this case $n_B = n_{Co} = 3$ and $J_{CoNb} = {}^1/_3(J_{AF} + 2J_F)$. If the values of $J_{AF} = -21.6$ cm^{-1} and $J_F = +15.4$ cm^{-1} estimated from the data for **1** and **2** are used in this equation, one can find the predicted value of $J_{Co-Nb}' = {}^1/_3(J_{AF} + 2J_F) = +3.1$ cm^{-1}, which is in good agreement with the experimental $J_{Co-Nb} = +3.5$ cm^{-1} obtained from the molecular field model for **3**. For **4** with M = Ni, the corresponding electronic configuration is $(t_{2g})^6(e_g)^2$. The number of unpaired electrons is again reduced by 1; hence, $n_B = n_{Ni} = 2$. The exchange coupling constant is given by $J_{Ni-Nb} = {}^1/_2(2J_F) = J_F$. Again, we can calculate the predicted value of J_{Ni-Nb}', which in this case is +15.4 cm^{-1} and compares well with the experimental +8.1 cm^{-1} found from the magnetic data of **4**.

4. Conclusions

In conclusion, we have obtained and characterized a series of new compounds **1**−**4** based on the [Nb^{IV}(CN)$_8$] moiety. All four compounds exhibit identical structures based on the symmetry-equivalent cyanido bridges and show long-range magnetic ordering below 24, 8, 6, and 14 K, respectively. The molecular field model analysis of the magnetic data has led to the values of exchange coupling constants J_{M-Nb} between the M^{II} and Nb^{IV} centers (listed in Table 4). The coupling constants J_{M-Nb} were found to increase monotonically on going from **1** to **4**, with a change of their character from antiferromagnetic for **1** and **2** to ferromagnetic for **3** and **4**. Additional magnetostructural analysis of the correlation between the decreasing number of unpaired electrons on the M^{II} center (5, 4, 3, and 2 for **1**−**4**, respectively) and the increasing trend in the exchange coupling constant showed that there are two main contributions to the total exchange coupling J_{M-Nb}: antiferromagnetic $J_{AF} = -21.6$ cm^{-1}, which originates from each singly occupied t_{2g} orbital of the M^{II} center, and ferromagnetic $J_F = +15.4$ cm^{-1}, originating from its e_g orbitals. The antiferromagnetic contribution to the total exchange coupling J_{M-Nb} is successively weakened with each additional electron pair on the t_{2g} level in the **1**−**4** row, resulting in a change of the strength and character of the total exchange coupling between M^{II} and Nb^{IV} and a change of the nature of the long-range magnetic ordering from ferrimagnetic in **1** and **2** to ferromagnetic in **3** and **4**. The observed trend is in agreement with expectations based on the rationale developed by Kahn and Verdaguer for magnetic Prussian Blue analogues.[4]

Table 4. Summary of the Molecular Field Calculations for **1**−**4**

	M^{II} center	number unpaired electrons on M^{II}	assumed coupling	T_c [K]	S_{M0}	g_M factor	J_{M-Nb} [cm^{-1}]
1	Mn	5	AF	23.8(5)	$^5/_2$	1.99(1)	−6.8(2)
2	Fe	4	AF	8.3(5)	2	2.163(2)	−3.1(2)
3	Co	3	F	5.9(5)	$^1/_2$	4.55(5)	+3.5(3)
4	Ni	2	F	13.4(5)	1	2.180(1)	+8.1(3)

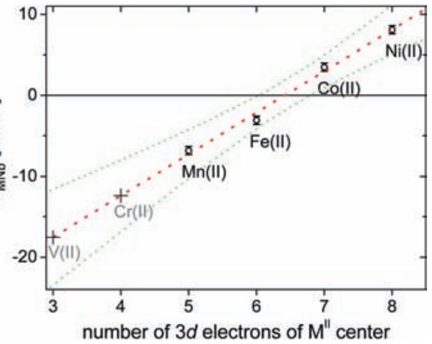

Figure 10. Linear fit of the "J_{M-Nb} vs number of 3d electrons" dependence ($R^2 = 0.9895$) for **1**−**4** (red dotted line) with 95% confidence limits (green dotted lines). Extrapolation gives predicted values of −12 and −18 cm^{-1} for possible Cr^{II} and V^{II} analogues, respectively.

This systematic study validates previous reports of antiferromagnetic interactions found in Mn^{II}−[M(CN)$_8$][12,13,15,31] and ferromagnetic ones in the Co^{II}−,[32] Ni^{II}−,[33] and Cu^{II}−[34]-[M(CN)$_8$]-based molecular magnets (with the restriction that the M^{II}−N−C angle is moderate). The values of the coupling constants J_{M-Nb} obtained in this study are also comparable with those reported in the literature. $J_{Mn-Nb} = -6.8$ cm^{-1} corresponds well with the −13.6 cm^{-1} value obtained for nonanuclear cyanido-bridged Mn$_6$Nb$_3$ clusters.[12a] On the other hand, the $J_{FeNb} = -3.1$ cm^{-1} value estimated for **2** is much lower than the value of −20 cm^{-1} deduced from fitting of the Ising model to the magnetic data of the Fe$_2$Nb chain recently reported by Venkatakrishnan et al.[12c] This discrepancy may arise from the completely different coordination environments of the Fe^{II} centers in both assemblies.

Moreover, extrapolation of the linear fit to the "J_{M-Nb} vs number of 3d electrons" dependence (Figure 10) enables the prediction of the exchange coupling for not yet reported Cr^{II} and V^{II} analogues of the $\{[M^{II}(pyrazole)_4]_2[Nb^{IV}(CN)_8]\cdot 4H_2O\}_n$ series: $J_{Cr-Nb} \approx -12$ cm^{-1} and $J_{V-Nb} \approx -17$ cm^{-1}, with T_c of the V^{II} analogue reaching the boiling point of liquid nitrogen. Studies in this field are in progress.

Acknowledgment. This work was financed by the Polish Ministry of Science and Higher Education within

---

(31) Song, Y.; Ohkoshi, S.-I.; Arimoto, Y.; Seino, H.; Mizobe, Y.; Hashimoto, K. *Inorg. Chem.* **2003**, *42*, 1848–1856.

(32) (a) Podgajny, R.; Bałanda, M.; Sikora, M.; Borowiec, M.; Spałek, L.; Kapusta, C.; Sieklucka, B. *Dalton Trans.* **2006**, *23*, 2801–2809. (b) Ohkoshi, S.-I.; Hamada, Y.; Matsuda, T.; Tsunobuchi, Y.; Tokoro, H. *Chem. Mater.* **2008**, *20*, 3048–3054.

(33) Nowicka, B.; Rams, M.; Stadnicka, K.; Sieklucka, B. *Inorg. Chem.* **2007**, *46*, 8123–8125.

(34) (a) Podgajny, R.; Chmiel, N. P.; Bałanda, M.; Tracz, P.; Gaweł, B.; Zając, D.; Sikora, M.; Kapusta, Cz.; Łasocha, W.; Wasiutyński, T.; Sieklucka, B. *J. Mater. Chem.* **2007**, *17*, 3308–3314. (b) Korzeniak, T.; Desplanches, C.; Podgajny, R.; Giménez-Saiz, C.; Stadnicka, K.; Rams, M.; Sieklucka, B. *Inorg. Chem.* **2009**, *48*, 2865–2872.

Research Project 0538/B/H03/2008/35 and partially supported by EU within IROP 2004-2006 (Integrated Regional Operational Programme), Priority II: Strengthening the Human Resources Development in Regions, Project MPD (Małopolskie Stypendium Doktoranckie). D.P. acknowledges Andrea Caneschi for hosting the short interdisciplinary external Ph.D. stay at the Laboratory of Molecular Magnetism, Department of Chemistry, Ugo Schiff, and INSTM Research Unit, University of Florence, Florence Italy, where the research was partly conducted. The stay was funded by EU within the MAGMANet project.

Supporting Information Available: PXRD diagram for **4**, crystallographic information files in CIF format and structural diagrams showing ASU and arrangement of pyrazole molecules in **1**−**4**, IR spectra and the results of ZFC/FC and ac magnetic measurements for **1**−**4**, and a table containing δ and φ dihedral angles for model and experimental eight-vertex geometries in **1**−**4**. This material is available free of charge via the Internet at http://pubs.acs.org.